minerals

MDPI

Article

Magmatic Controls on Contrasting Molybdenum Fertility of Caledonian Granitoids in Eastern Guangxi, South China

Lian Mo [1,2], Yizhi Liu [1,*], Guicong Fang [1], Zonglin Jiang [3], Er Wu [2], Lei Qin [2] and Bachtiar Wahyu Mutaqin [4]

1 Guangxi Key Laboratory of Hidden Metallic Ore Deposits Exploration, Guilin University of Technology, Guilin 541006, China; 13768336684@163.com (L.M.); fanggcong@163.com (G.F.)
2 School of Civil Engineering, Nanning College of Technology, Guilin 541006, China; 18078351883@163.com (E.W.); 17307735460@163.com (L.Q.)
3 Guangxi Institute of Geological Survey and Research, Guilin 541003, China; zk0501110@126.com
4 Coastal and Watershed Research Group, Faculty of Geography, Universitas Gadjah Mada, Yogyakarta 55281, Indonesia; mutaqin@ugm.ac.id
* Correspondence: liuyizhiglut@glut.edu.cn

Abstract

Caledonian hydrothermal vein-type Mo deposits are largely restricted to eastern Guangxi, South China, yet the magmatic controls on molybdenum (Mo) mineralization remain poorly constrained. The adjacent Guiling (Mo–mineralized) and Daning (Mo–barren) plutons in this region represent a natural pair for deciphering these issues. Zircon U–Pb dating, whole-rock geochemistry, and mineralogical characteristics indicate that the Daning pluton (~440 Ma) is an I-type granite, whereas the younger Guiling pluton (~425 Ma) is a more evolved I-type granite, with higher SiO_2 contents (avg. 71.17 wt.% vs. 65.88 wt.%), stronger negative Eu anomalies (avg. 0.53 vs. 0.63), lower Nb/Ta ratios (avg. 6.5 vs. 9.9), and Zr/Hf ratios (avg. 30.6 vs. 33.4), as well as higher Rb/Sr ratios (avg. 3.6 vs. 1.1). Sr–Nd–Hf isotopes are consistent with a Paleoproterozoic crustal source for both plutons, whereas coeval mafic microgranular enclaves in the Guiling pluton exhibit positive $\varepsilon_{Nd}(t)$ values (+3.43 to +3.58), providing evidence for mantle input. Biotite geochemistry shows that the Guiling pluton is enriched in F and Cl, as reflected by lower $\log(f_{H2O}/f_{HF})^{fluid}$ values and higher $\log(f_{H2O}/f_{HCl})^{fluid}$ values. Our integrated study suggests that the Daning and Guiling plutons were emplaced in an intracontinental orogenic setting during the transition from compression to extension, but the more pronounced extension facilitated a greater input of mantle-derived heat and volatiles into the Guiling pluton, favoring Mo enrichment. However, the similar biotite crystallization temperatures and moderate oxygen fugacities of both plutons suggest that these factors were not the decisive factors. Collectively, we propose that the contrasting Mo fertility between the two plutons reflects the interplay of magmatic and structural factors. Magmatically, crust–mantle source mixing, high degrees of fractionation, and volatile enrichment promoted Mo concentration, whereas ductile shear zones likely served as fluid conduits that facilitated mineralization. Accordingly, the southwestern segment of the Yingyangguan (YYG) ductile shear zone between the Daning and Guiling plutons could be a prospective target for Mo prospecting in eastern Guangxi.

Keywords: biotite; Caledonian I-type granitoids; crust–mantle hybrid source; molybdenum mineralization; eastern Guangxi

Check for updates

Academic Editor: Pierfranco Lattanzi

Received: 6 June 2026
Revised: 8 July 2026
Accepted: 14 July 2026
Published: 16 July 2026

1. Introduction

Molybdenum (Mo) is critical for China's advanced alloy and clean energy industries. Large-scale Yanshanian W–Sn–Mo mineralization occurs in South China (Figure 1) [1], but Caledonian metallogenesis in this region is relatively limited [2]. It is noteworthy that Caledonian Mo deposits in South China are predominantly sedimentary-type (SMT), whereas hydrothermal vein-type (HVT) Mo deposits are largely restricted to eastern Guangxi (Figure 1a) [3]. Critically, HVT Mo deposits are genetically linked to granites [4,5], and highly fractionated granitic magmatism drives Mo mobilization and enrichment in the continental crust [6,7]. Previous studies have investigated Mo mineralization in terms of source composition and magma differentiation [4,8,9], as well as emplacement conditions such as temperature, pressure, oxygen fugacity, and volatiles (e.g., F, Cl) [6,10]. Nevertheless, a lack of suitable comparative case studies has left the collective roles of these factors in Mo mineralization poorly constrained.

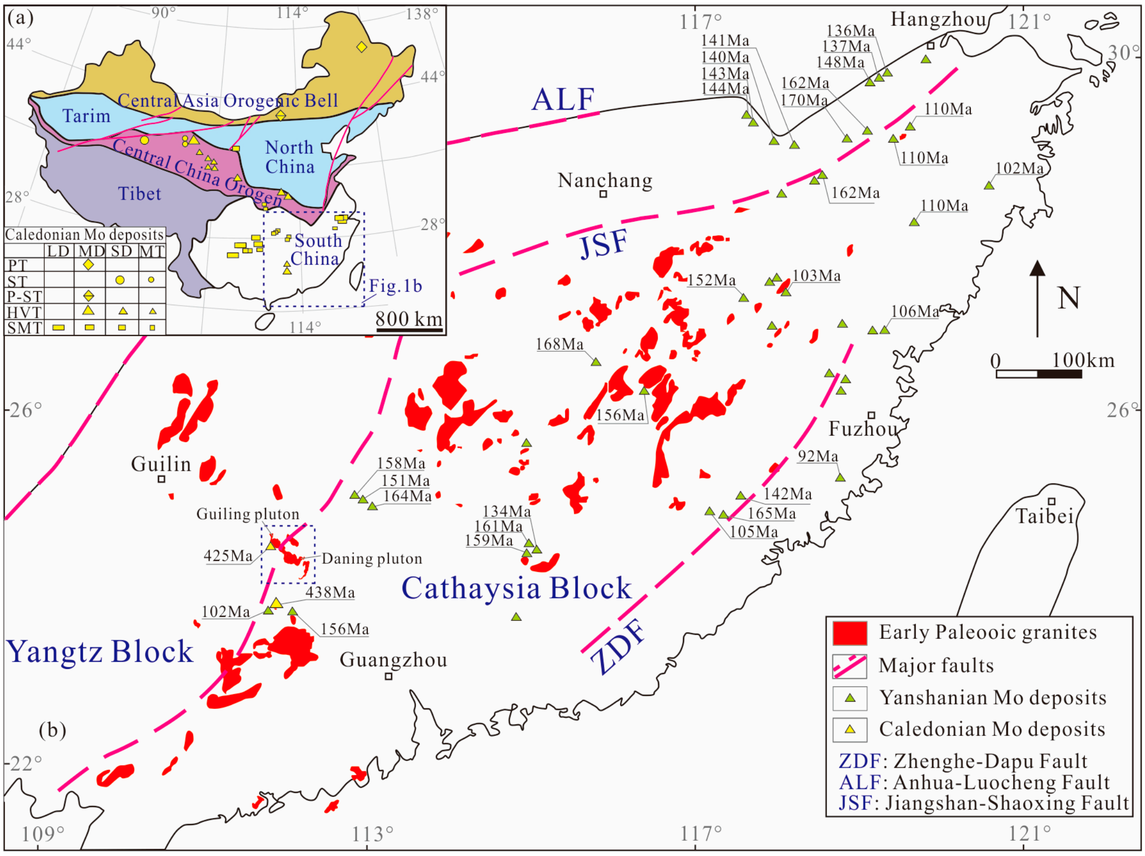

Figure 1. (**a**) Spatial distribution of Caledonian molybdenum deposits in China (modified after [4,5]), and (**b**) simplified geological map of the South China Block showing the distribution of early Paleozoic granitic and molybdenum deposits (base map modified after [11,12]). Deposit scale: LD—large; MD—medium; SD—small; MT—mineralized occurrence. Deposit types: PT—porphyry type; ST—skarn type; P-ST—porphyry–skarn type; HVT—hydrothermal (vein) type; SMT—sedimentary (metamorphic) type.

The Caledonian granitoids exposed in eastern Guangxi provide an excellent opportunity to investigate these processes (Figure 1b). Among them, the spatially adjacent Daning and Guiling plutons exhibit contrasting Mo mineralization: the smaller Guiling pluton hosts a small-scale quartz vein-type Mo deposit (avg. Mo grade 0.12%; contained Mo, 1080.53 t) [13], whereas the larger Daning pluton shows no significant Mo mineralization, leaving its potential unclear. This association of mineralized and barren plutons represents a natural pair for deciphering how physicochemical conditions during magmatic evolution control Mo mineralization. Here, we present a systematic comparison of the Guiling (Mo-mineralized) and Daning (Mo-barren) plutons using geochronology, whole-rock geochemistry, isotopic geochemistry, and biotite mineral chemistry. To better understand the controls on the contrasting Mo mineralization and its link to magmatic processes, we investigated the petrogenesis, source characteristics, degree of fractionation, and biotite crystallization conditions (T, P, fO_2, and F–Cl contents) of both plutons. Our integrated approach offers insights for evaluating the Mo metallogenic potential of similar Caledonian granitoids throughout eastern Guangxi.

2. Geological Setting

The exposed strata in eastern Guangxi range from the Neoproterozoic Danzhou Group and the Nanhua and Sinian systems to the Paleozoic Cambrian (with the Silurian and Ordovician missing), Devonian, and Carboniferous systems, as well as the Mesozoic Cretaceous System (Figure 2). Regional folds and structures predominantly trend NE–NNE, accompanied by Caledonian Yingyangguan (YYG) and Longwu (LW) ductile shear zones. Magmatic activity was most significant during the Caledonian and Yanshanian periods. In particular, the Caledonian granites (emplaced at 440–420 Ma) [13–16] cover an extensive area of ~1000 km^2. Spatially, the LW ductile shear zone is situated between the Guposhan and Guiling plutons, whereas the YYG ductile shear zone lies between the Guiling and Daning plutons.

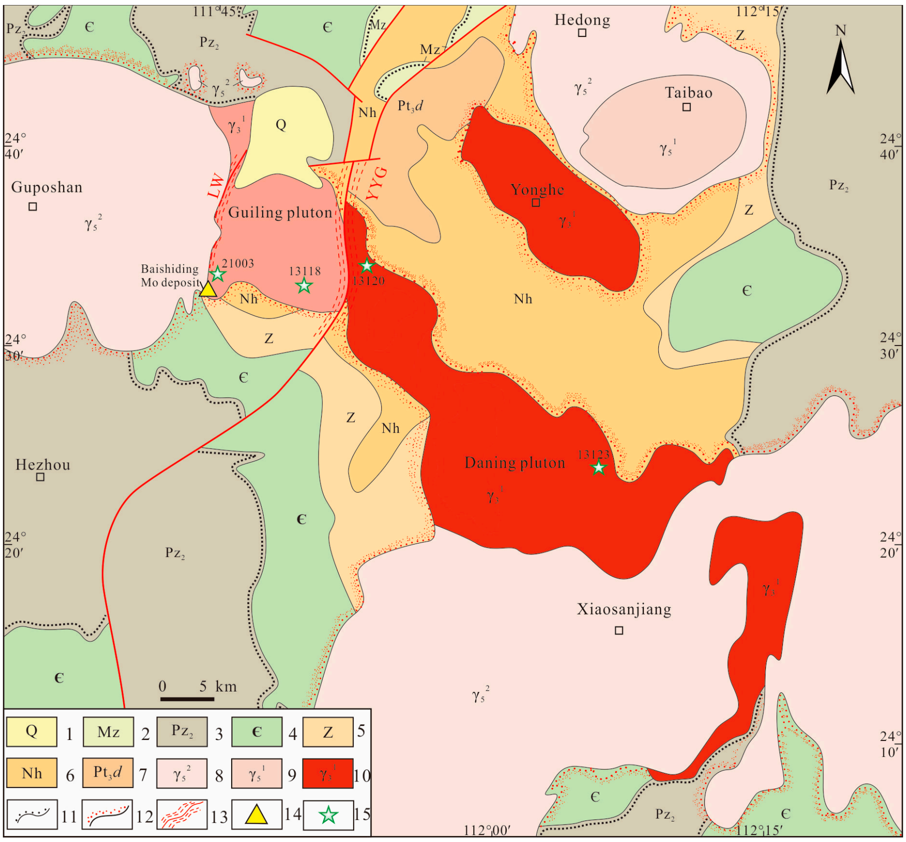

Figure 2. Geological sketch map of eastern Guangxi (modified after [16]): 1—Quaternary; 2—Mesozoic; 3—Upper Paleozoic; 4—Cambrian; 5—Sinian; 6—Nanhuan; 7—Danzhou Group; 8—Yanshanian granite; 9—Indosinian granite; 10—Caledonian granite; 11—angular unconformity; 12—thermal contact metamorphic zone; 13—ductile shear zone and fault; 14—Caledonian molybdenum deposit; 15—sampling location. YYG—Yingyangguan ductile shear zone; LW—Longwu ductile shear zone.

The Guiling and Daning plutons are typical representatives of the Caledonian granites in the study area (Figure 2). Both plutons intrude into the Precambrian strata, displaying irregularly curved contact boundaries (Figure 3a,b), and commonly contain mafic microgranular enclaves (MME) of varying sizes, which show sharp contacts with their host granites (Figure 3c,e). Although spatially adjacent, the two plutons differ markedly in scale and mineralization characteristics: the NNE-trending, "b"-shaped Guiling pluton covers ~144 km^2 and hosts a small-scale quartz vein-type molybdenum deposit (molybdenite Re–Os age of 424.6 ± 5.7 Ma) [13]. By contrast, the NW–SE-trending, reverse "L"-shaped Daning pluton (spatially intruded by the nearly EW-trending Yanshanian Lianyang granite) has an exposed area of ~426 km^2, and no contemporaneous Mo mineralization has been reported. In recent years, increasing evidence for Caledonian Mo mineralization has been documented in eastern Guangxi, including the Shedong HVT Mo deposit (437.8 ± 3.1 Ma) and the Wujie HVT Mo deposit (438.4 ± 3.3 Ma) [17,18], suggesting that the Caledonian period was also a significant Mo metallogenic epoch in South China.

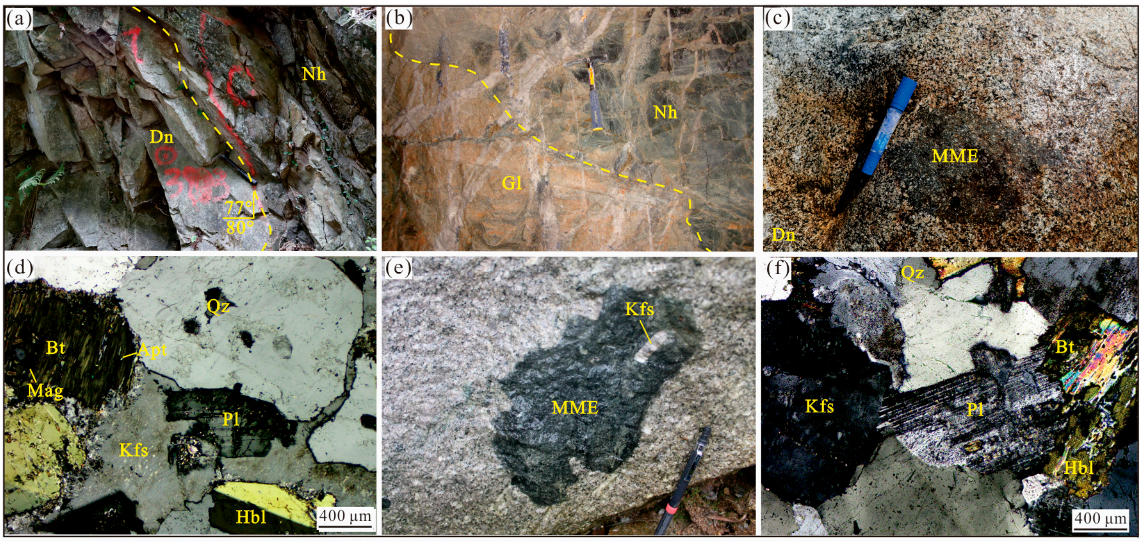

Figure 3. Field photographs and photomicrographs from the Daning and Guiling plutons. (**a**,**b**) Intrusive contact between the granites and the Precambrian strata, showing irregularly curved contact boundaries; (**c**,**d**) outcrop and photomicrograph (+) of granodiorite from the Daning pluton (Dn); (**e**,**f**) outcrop and photomicrograph (+) of amphibole-bearing biotite monzogranite from the Guiling pluton (Gl). Nh—the Nanhua System; MME—mafic microgranular enclaves; Hbl—hornblende; Bt—biotite; Qz—quartz; Pl—plagioclase; Kfs—K-feldspar; Mag—magnetite; Apt—apatite.

3. Sample Characteristics and Analytical Methods

3.1. Sample Characteristics

Four representative granitoid samples (13123, 13120, 13118, and 21003) were collected from the Daning and Guiling plutons for petrographic observations and subsequent geochemical analyses (Figure 2).

The Daning pluton is composed mainly of medium- to fine-grained granodiorite with abundant irregular mafic microgranular enclaves (Figure 3c). The grayish–white rock has a medium- to fine-grained granitic texture and massive structure. Its main mineral assemblage consists of plagioclase (44–46 vol.%), K-feldspar (20–25 vol.%), quartz (20–23 vol.%), biotite (5–7 vol.%), and amphibole (5–8 vol.%), with accessory magnetite, titanite, zircon, and apatite (Figure 3d). K-feldspar shows weak kaolinization. Plagioclase grains commonly display polysynthetic twinning, with straight and well-defined twin lamellae, indicative of a magmatic origin. Biotite occurs mainly as subhedral tabular crystals enclosing apatite and magnetite inclusions.

The Guiling pluton is mainly composed of amphibole-bearing biotite monzogranite with abundant mafic microgranular enclaves (Figure 3e). The light grayish–white rock has a medium- to fine-grained porphyritic texture and massive structure. The main mineral assemblage consists of plagioclase (30–32 vol.%), K-feldspar (35–38 vol.%), quartz (25–27 vol.%), biotite (3–4 vol.%), and amphibole (4–5 vol.%), with accessory zircon, titanite, and apatite (Figure 3f). Plagioclase crystals also exhibit well-developed polysynthetic twinning, confirming a magmatic origin. Biotite occurs as subhedral to scaly crystals, with inclusions of apatite.

3.2. Analytical Methods

Zircon U–Pb dating, Hf isotope analysis, and biotite compositional analysis were performed at the Guangxi Key Laboratory of Hidden Metallic Mineral Exploration, Guilin University of Technology.

Zircon U–Pb dating was performed using an Agilent 7900 ICP–MS (Agilent Technologies, Santa Clara, CA, USA) with a GeoLas HD 193 nm ArF excimer laser ablation system (Coherent GmbH, Göttingen, Germany). Analyses employed a 24–32 μm spot size and 6 Hz repetition rate, with He carrier gas and Ar make-up gas. Zircon 91500 (1064 ± 7 Ma) was the external standard for fractionation calibration, with GJ–1 (599.8 ± 1.7 Ma) [19] and Plešovice (337 ± 0.37 Ma) [20] as reference standards. Common Pb correction followed Andersen [21]. Data were reduced using ICPMSDataCal 8.3, and ages and concordia diagrams were obtained with Isoplot 3. Uncertainties: 1σ for individual analyses, 2σ for weighted mean ages. Detailed procedures are described in Huang et al. [22].

Zircon Lu–Hf analyses were performed on the same zircons dated by U–Pb, with ablation pits placed within the same textural domains. Analyses used a Neptune MC–ICP–MS with a New Wave UP213 UV laser ablation system (Thermo Fisher Scientific, Waltham, MA, USA), with He carrier gas and N_2 introduced post-ablation to enhance Hf sensitivity. Single-spot ablation used a 20 Hz repetition rate and a 32 to 45 μm spot size. Standards GJ–1 and Plešovice gave $^{176}Hf/^{177}Hf$ ratios of 0.282021 ± 0.000008 (2σ) and 0.282481 ± 0.000008 (2σ), respectively. $\varepsilon_{Hf}(t)$ and model ages were calculated using a ^{176}Lu decay constant of 1.867×10^{-11} yr^{-1} and chondritic ($^{176}Hf/^{177}Hf$ = 0.282772, $^{176}Lu/^{177}Hf$ = 0.0332) and depleted mantle ($^{176}Hf/^{177}Hf$ = 0.28325, $^{176}Lu/^{177}Hf$ = 0.0384) values. Detailed procedures follow Huang et al. [22].

Biotite analyses were performed using a JEOL JXA–8230 electron microprobe (EPMA) (JEOL Ltd., Tokyo, Japan) under the following conditions: an accelerating voltage of 15 kV, a beam current of 20 nA, a beam diameter of 2–5 μm, with peak/background counting times of 20/10 s and ZAF correction. The detection limit for major elements was 0.01 wt.%. Reference standards from the Institute of Mineral Resources, Chinese Academy of Geological Sciences, included albite (Na, Si, Al), hematite (Fe), forsterite (Mg), phlogopite (K), rutile (Ti), manganite (Mn), topaz (F), and apatite (Ca, Cl). Cation numbers were normalized to 22 oxygen atoms. The Fe^{2+} and Fe^{3+} contents of biotite were calculated following the method of Lin and Peng [23]. The solidification pressures were calculated using the equations of Uchida [24]. The fugacity ratios $\log(f_{H2O}/f_{HF})$, $\log(f_{H2O}/f_{HCl})$, and $\log(f_{HF}/f_{HCl})$ of melts/fluids equilibrated with biotite were calculated using the equations of Munoz [25] and the F–Cl–OH exchange partition coefficients between biotite and hydrothermal fluid [26]. Detailed analytical procedures follow Mo et al. [27].

4. Analytical Results

4.1. Geochronology

LA–ICP–MS zircon U–Pb dating was performed on three representative samples (13120, 13123, and 13118) collected from the Daning and Guiling plutons. The analytical results are summarized in Table S1.

Zircons from sample 13120 of the Daning pluton have Th/U ratios (ranging from 0.30 to 0.64) > 0.1, indicating a typical magmatic origin. Analyses of 18 zircon grains yielded $^{206}Pb/^{238}U$ ages ranging from 423 to 460 Ma (Table S1). All data points plot on or near the concordia curve (Figure 4a), giving a weighted mean $^{206}Pb/^{238}U$ age of 437.6 ± 5.6 Ma.

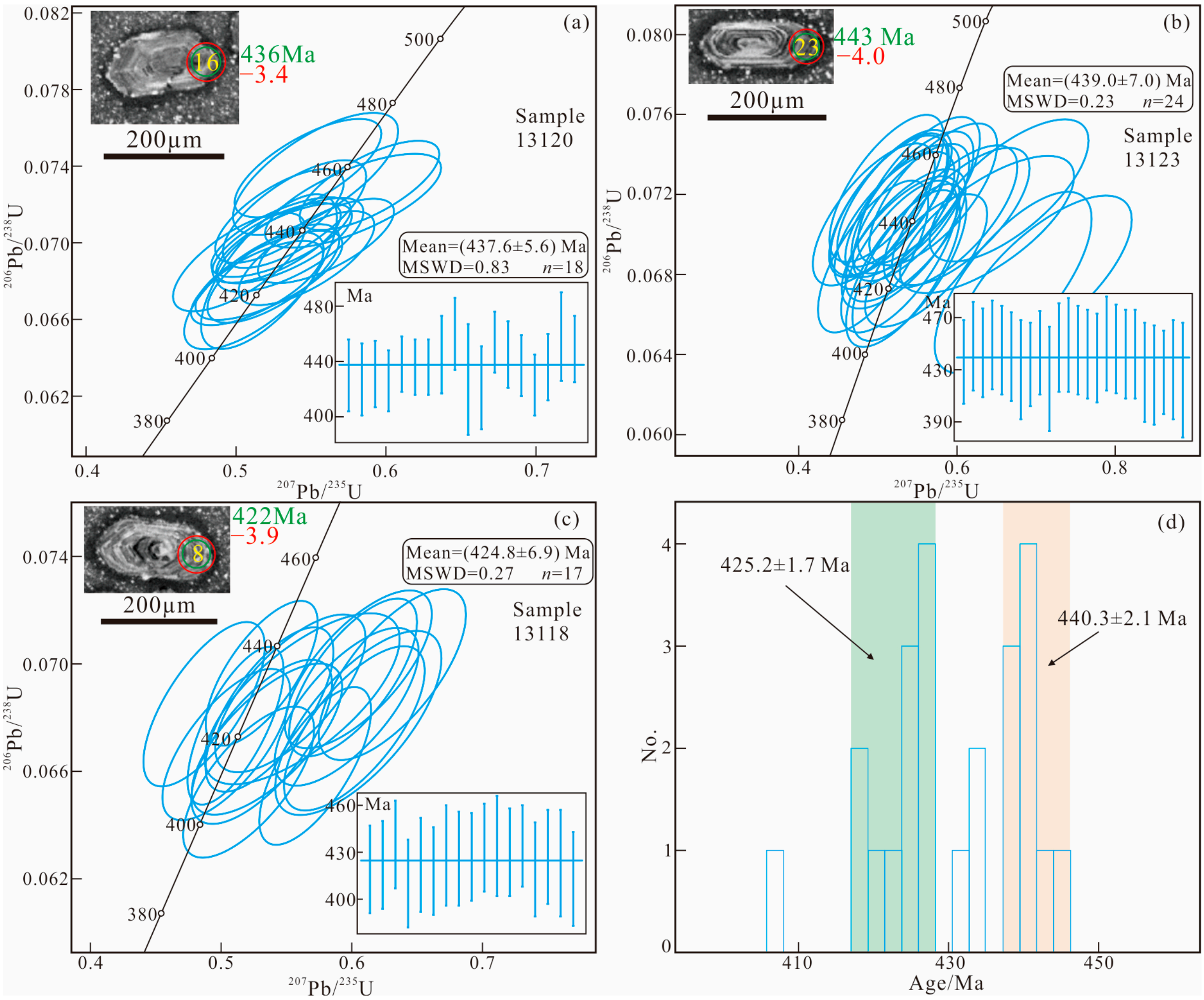

Figure 4. Zircon U–Pb concordia diagrams (**a**–**c**) and age distribution histogram (**d**) for the Daning and Guiling plutons. Green circles with font indicate U–Pb ages, red indicate εHf(t) values, and yellow indicate analytical spots on zircon CL images.

Zircons from sample 13123 of the Daning pluton have Th/U ratios (ranging from 0.33 to 1.92) > 0.1, indicating a typical magmatic origin. Analyses of 24 zircon grains gave $^{206}Pb/^{238}U$ ages ranging from 421 to 450 Ma (Table S1). All data points plot on or near the concordia curve (Figure 4b), yielding a weighted mean $^{206}Pb/^{238}U$ age of 439.0 ± 7.0 Ma.

Zircons from sample 13118 of the Guiling pluton have Th/U ratios (ranging from 0.54 to 1.73) > 0.1, indicating a typical magmatic origin. Analyses of 17 zircon grains yielded $^{206}Pb/^{238}U$ ages ranging from 410 to 435 Ma (Table S1). All data points plot on or near the concordia curve (Figure 4c), giving a weighted mean $^{206}Pb/^{238}U$ age of 424.8 ± 6.9 Ma.

Integrating published geochronological data [16] with our new ages (Figure 4d) yields peak crystallization ages of 440.3 ± 2.1 Ma for the Daning pluton and 425.2 ± 1.7 Ma for the Guiling pluton.

4.2. Whole-Rock Geochemistry

Whole-rock major- and trace-element data for the Daning and Guiling plutons were compiled from published studies [15,28–33] and are listed in Table S2. Major element data exhibit generally low loss on ignition (LOI) values (<2%; one outlier at 2.73%), and most major elements display negative correlations with SiO_2 (Figure 5a–g), suggesting that post-magmatic alteration did not significantly modify the whole-rock compositions.

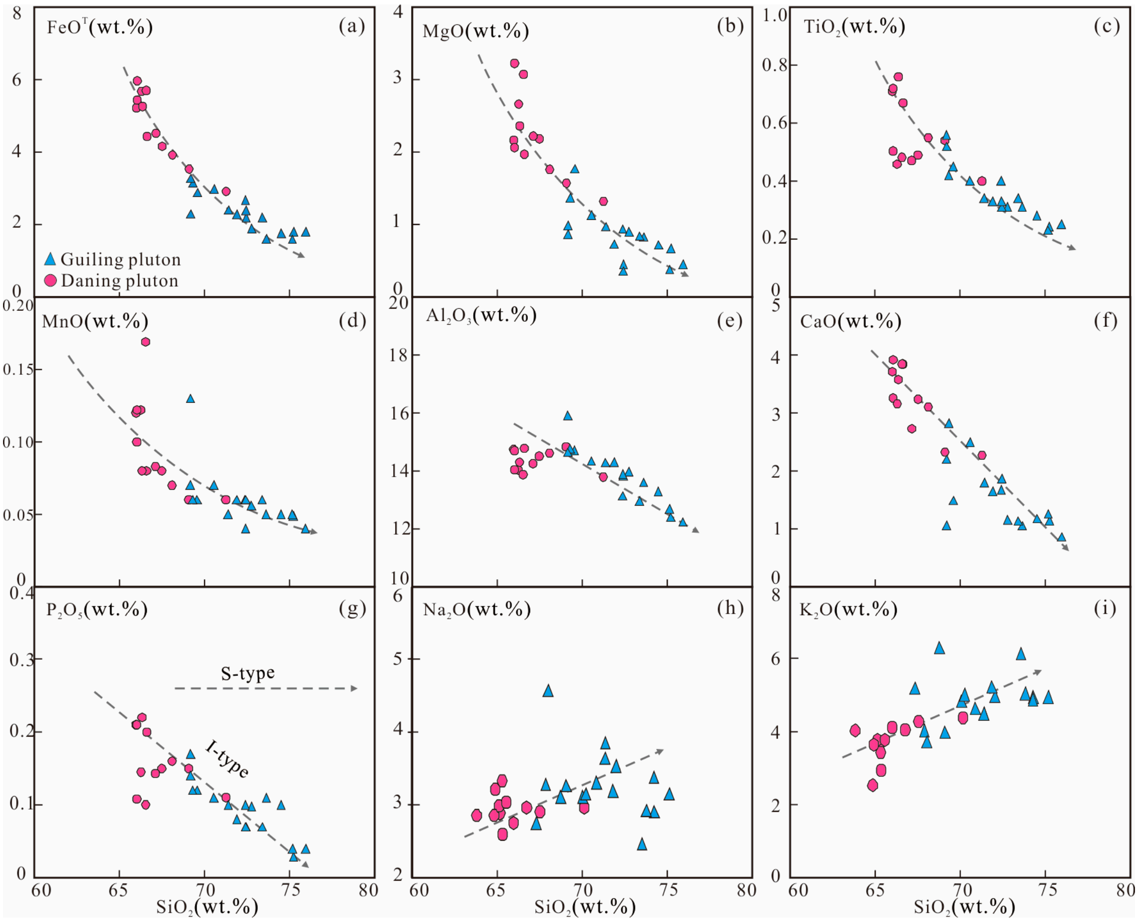

Figure 5. Harker diagrams of major elements for the Daning and Guiling plutons. (**a**) SiO_2–FeO^T diagram; (**b**) SiO_2–MgO diagram; (**c**) SiO_2–TiO_2 diagram; (**d**) SiO_2–MnO diagram; (**e**) SiO_2–Al_2O_3 diagram; (**f**) SiO_2–CaO diagram; (**g**) SiO_2–P_2O_5 diagram; (**h**) SiO_2–Na_2O diagram; (**i**) SiO_2–Ka_2O diagram.

The Daning pluton has low SiO_2 (63.82–70.15 wt.%, avg. 65.88 wt.%), moderate Na_2O (2.59–3.33 wt.%, avg. 2.94 wt.%) and K_2O (2.54–4.40 wt.%, avg. 3.73 wt.%), and low CaO (2.23–3.84 wt.%, avg. 3.18 wt.%), TiO_2 (0.40–0.76 wt.%, avg. 0.56 wt.%), FeO^T (2.96–6.08 wt.%, avg. 4.83 wt.%), MgO (1.32–3.22 wt.%, avg. 2.21 wt.%), and P_2O_5 (0.10–0.22 wt.%, avg. 0.16 wt.%). In contrast, the Guiling pluton shows higher SiO_2 (67.33–75.13 wt.%, avg. 71.17 wt.%) and lower CaO (0.85–2.76 wt.%, avg. 1.54 wt.%), TiO_2 (0.23–0.56 wt.%, avg. 0.35 wt.%), FeO^T (1.60–3.33 wt.%, avg. 2.34 wt.%), MgO (0.36–1.77 wt.%, avg. 0.85 wt.%), and P_2O_5 (0.03–0.17 wt.%, avg. 0.09 wt.%). The TAS, SiO_2–K_2O, and A/CNK–A/NK diagrams (Figure 6a–c) classify the Daning pluton as a granodiorite, with calc–alkaline to high-K calc–alkaline affinity and metaluminous to weakly peraluminous compositions (A/CNK = 0.93–1.10, avg. 0.98). In contrast, the Guiling pluton plots in the granite field, with high-K calc–alkaline to shoshonitic affinity and metaluminous to weakly peraluminous compositions (A/CNK = 0.94–1.15, avg. 1.03). Overall, the transition from the Daning pluton to the Guiling pluton is marked by increasing SiO_2, Na_2O, and K_2O, and decreasing FeO^T, MgO, TiO_2, MnO, Al_2O_3, CaO, and P_2O_5 (Figure 5).

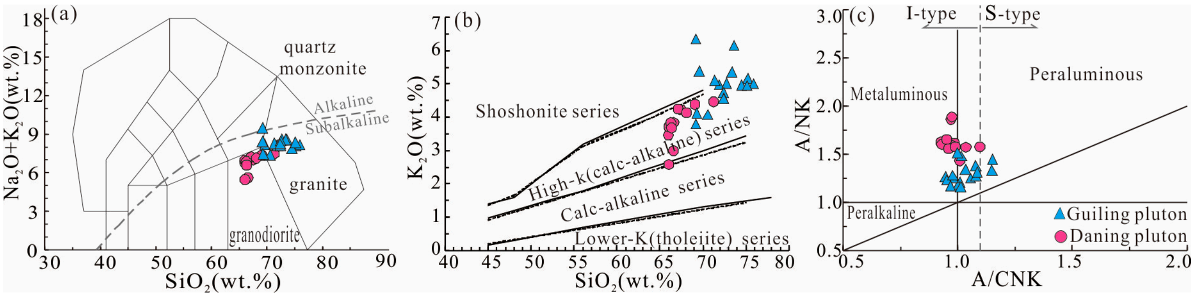

Figure 6. (**a**) TAS diagram (after [34]), (**b**) SiO_2–K_2O diagram (after [35]), and (**c**) A/CNK–A/NK diagram (after [34]) for the Daning and Guiling plutons.

The primitive mantle-normalized spider diagram (Figure 7a) shows that both plutons exhibit positive Rb, Th, U, and Ta anomalies, as well as negative Ba, Sr, Nb, P, and Ti anomalies, along with minor negative Zr anomalies. Compared to the Daning pluton, the Guiling pluton has lower K/Rb, Nb/Ta, and Zr/Hf ratios (avg. 174.7 vs. 142.6; 9.9 vs. 6.5; 33.4 vs. 30.6, respectively), whereas its Rb/Sr ratio is higher (avg. 3.6 vs. 1.1). The chondrite-normalized REE patterns (Figure 7b) show that both plutons have similar seagull-shaped patterns, with LREE enrichment and HREE depletion. Notably, the Guiling pluton displays a more pronounced negative Eu anomaly (δEu value of avg. 0.53 vs. 0.63) and lower total REE content (avg. 150.1×10^{-6}) than the Daning pluton (avg. 192.9×10^{-6}).

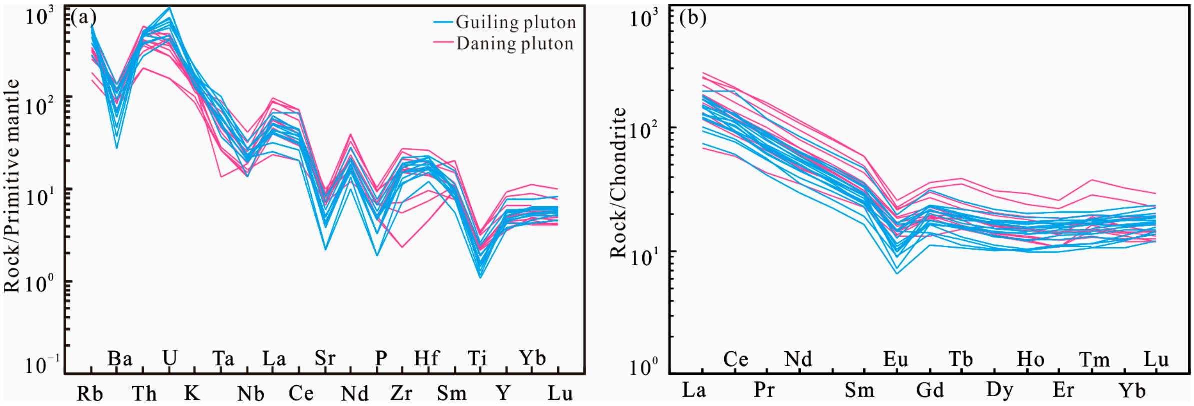

Figure 7. (**a**) Primitive mantle-normalized trace element spider diagram; (**b**) chondrite-normalized REE pattern diagram for the Daning and Guiling plutons. Normalization values are from [36].

4.3. Hf–Nd Isotope Characteristics

Zircon Hf isotope analysis results (Table S3) show consistent compositions for the Daning and Guiling plutons. The Daning pluton (analyses of 22 zircons) yields $\varepsilon_{Hf}(t)$ values of −4.4 to −1.2 (avg. −3.1) and two-stage depleted mantle model ages (T_{2DM}) of 1508–1695 Ma (avg. 1625 Ma). The Guiling pluton (analyses of six zircons) yields $\varepsilon_{Hf}(t)$ values of −4.6 to −2.6 (avg. −3.4) and T_{2DM} values of 1574–1702 Ma (avg. 1631 Ma). On the $\varepsilon_{Hf}(t)$ vs. age diagram (Figure 8a), samples from both plutons plot between the chondritic mantle and the Paleoproterozoic crustal evolution domain of South China, indicating derivation mainly from partial melting of Paleoproterozoic crustal materials.

https://doi.org/10.3390/min16070739

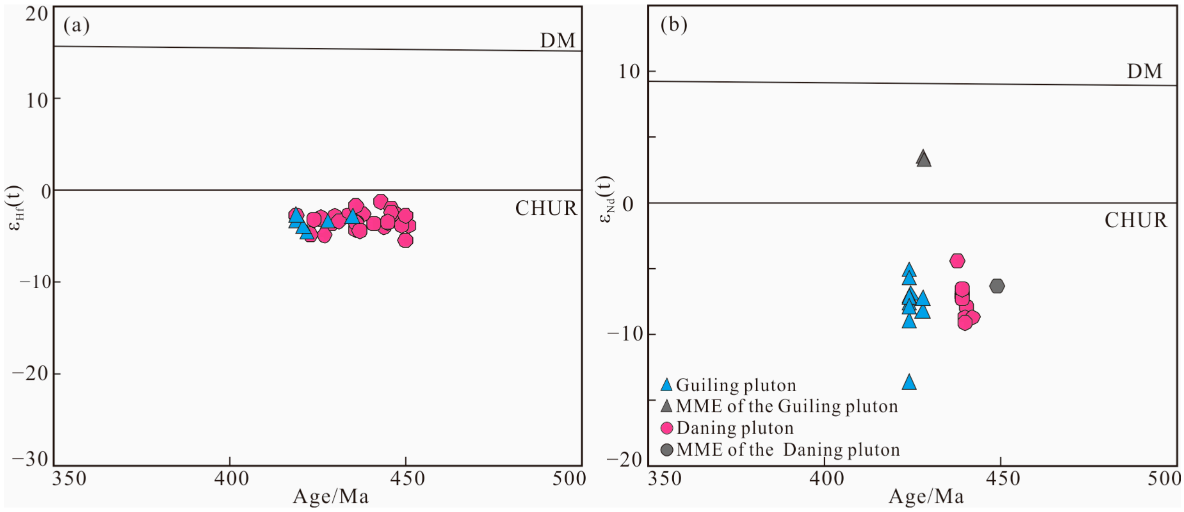

Figure 8. (**a**) $\varepsilon_{Hf}(t)$ vs. age diagram (after [1]) and (**b**) $\varepsilon_{Nd}(t)$ vs. age diagram (after [37]) for the Daning and Guiling plutons. MME—mafic microgranular enclaves.

Published whole-rock Nd isotopic data [31–33] for the two plutons were compiled (data sources are listed in Table S4). The Daning pluton yields $\varepsilon_{Nd}(t)$ values of −9.1 to −6.5 (avg. −7.9) and T_{2DM} values of 1713–1914 Ma (avg. 1817 Ma), whereas the Guiling pluton yields $\varepsilon_{Nd}(t)$ values of −13.6 to −5.0 (avg. −7.7) and T_{2DM} values of 1584–2251 Ma. Both plutons plot near the Paleoproterozoic crustal evolution domain on the $\varepsilon_{Nd}(t)$ vs. age diagram (Figure 8b), consistent with a Paleoproterozoic crustal source. Notably, mafic microgranular enclaves (MME) of the Daning pluton have $\varepsilon_{Nd}(t)$ values of −6.3 and T_{2DM} values of 1701 Ma, consistent with those of their host rocks and suggesting they are cognate schlieren. In contrast, contemporaneous enclaves of the Guiling pluton exhibit positive $\varepsilon_{Nd}(t)$ values of +3.4 to +3.6 (avg. +3.5) and younger T_{2DM} ages of 911–923 Ma (avg. 917 Ma), indicating a depleted mantle source. Thus, mantle-derived materials contributed significantly to the Guiling pluton.

4.4. Biotite Mineral Chemistry Characteristics

EPMA results of biotite composition (Table S5) reveal significant compositional differences between the two plutons. The Daning pluton has higher Al_2O_3 (13.25–16.08 wt.%, avg. 14.37 wt.%) but lower TiO_2 (1.21–4.02 wt.%, avg. 2.94 wt.%), MgO (10.06–16.08 wt.%, avg. 12.28 wt.%), FeO^T (16.38–20.89 wt.%, avg. 20.06 wt.%), F (0.06–1.11 wt.%, avg. 0.64 wt.%), and Cl (0.01–0.06 wt.%, avg. 0.03 wt.%) than the Guiling pluton (Al_2O_3: 13.42–14.73 wt.%, avg. 13.88 wt.%; TiO_2: 1.60–4.00 wt.%, avg. 3.09 wt.%; FeO^T: 20.35–24.45 wt.%, avg. 22.05 wt.%; F: 0.30–1.58 wt.%, avg. 0.65 wt.%; Cl: 0.05–0.15 wt.%, avg. 0.10 wt.%; MgO: 9.77–13.04 wt.%, avg. 10.82 wt.%). All analyzed biotite grains are magnesian (Figure 9a). Although the Guiling pluton is more enriched in F and Cl but more depleted in Mg than the Daning pluton (Figure 9b–d), biotite crystallization temperatures (T_{Bt}) and oxygen fugacities (fO_2) are similar between the two plutons. Both plutons have T_{Bt} ranges of 548–745 °C (avg. 680 °C) for Daning and 586–724 °C (avg. 682 °C) for Guiling, and average fO_2 values of −17.58 and −17.47, respectively (Figure 9e,f).

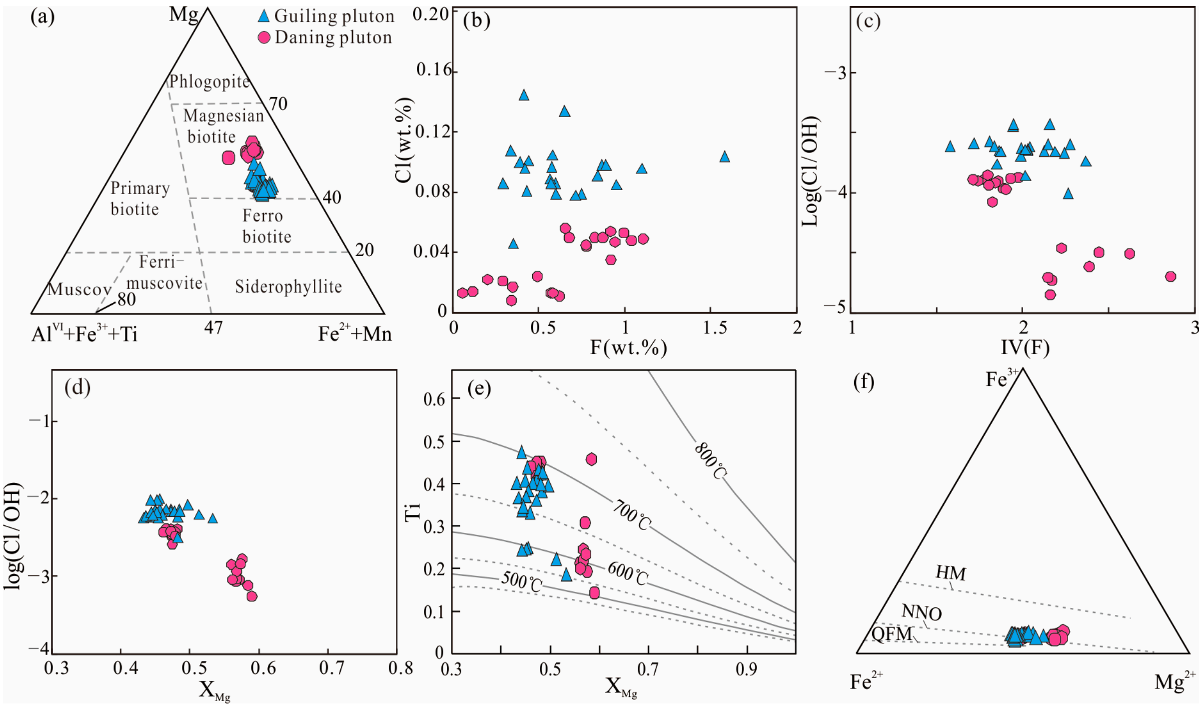

Figure 9. (**a**) Mg–Al^{VI} + Fe^{3+} + Ti–Fe^{2+} + Mn diagram (after [38]); (**b**) F–Cl diagram; (**c**) IV(F)–log(F/Cl) diagram; (**d**) log(Cl/OH)–X_{Mg} diagram; (**e**) Ti–in–biotite crystallization temperature diagram (after [39]); and (**f**) Fe^{3+}–Fe^{2+}–Mg^{2+} diagram (after [40]) for biotite from the Daning and Guiling plutons. HM: hematite–magnetite; NNO: nickel–nickel oxide; QFM: fayalite–quartz–magnetite.

These values plot near the NNO (nickel–nickel oxide) buffer, indicating moderate fO_2. However, solidification pressures are higher for the Daning pluton (149 MPa) than for the Guiling pluton (114 MPa).

5. Discussion

5.1. Granite Petrogenesis

Granites are genetically classified into M, A, I, and S types [41–43]. M-type granites are extremely rare and typically recognized as plagiogranites associated with ophiolites [41]. The Caledonian granites in eastern Guangxi are mainly granodiorites and monzogranites (Figures 3e,f and 6a), with distinctly negative $\varepsilon_{Nd}(t)$ values (avg. −7.9 to −7.7) and $\varepsilon_{Hf}(t)$ values (avg. −3.4 to −3.1). This precludes direct derivation from juvenile mantle-derived materials, ruling out an M-type affinity.

A-type granites typically form in anhydrous, alkaline, anorogenic environments and contain alkaline mafic minerals such as arfvedsonite–riebeckite and aegirine–augite. They are characterized by high Si, Na, K, (K_2O + Na_2O)/Al_2O_3 and FeO^T/MgO (>10) ratios, as well as low Ca, Mg and Al. Diagnostic trace element criteria include high Ga and Zr, low Co and Cr, a pronounced negative Eu anomaly, 10000 Ga/Al > 2.6, Zr + Nb + Ce + Y > 350 × 10^{-6}, and crystallization temperatures (Tzr) > 800 °C [42,43]. The studied samples lack alkaline minerals (Figure 3c–f), belong to the high-K calc–alkaline to shoshonitic series (Figure 6b), and have moderate negative Eu anomalies (avg. δEu = 0.57; Figure 7b). Their ratios of FeO^T/MgO (avg. 3.48), 10000 Ga/Al (avg. 2.41), and Zr + Nb + Ce + Y (avg. 273 × 10^{-6}) are all well below the typical A-type granite thresholds. On the Zr + Nb + Ce + Y vs. K_2O + Na_2O + CaO and SiO_2 vs. Y diagrams (Figure 10a,b), most analyses from both plutons plot outside the A-type granite field, excluding an A-type affinity.

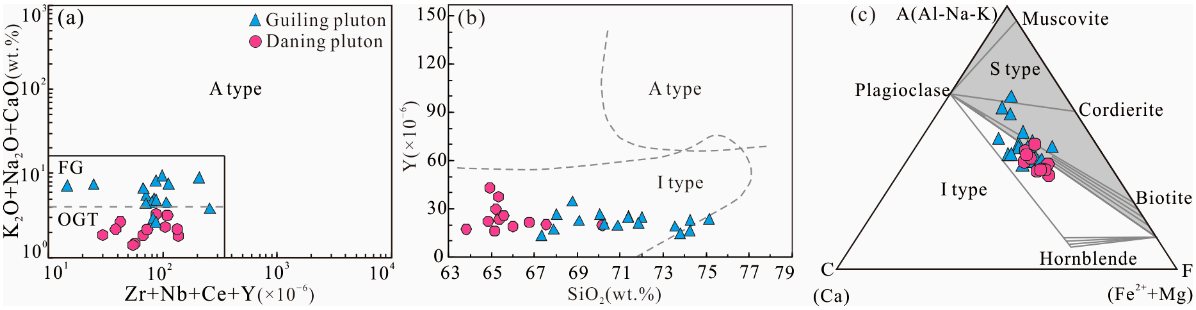

Figure 10. (**a**) (Zr + Nb + Ce + Y) vs. (K_2O + Na_2O + CaO) diagram (after [42]), (**b**) SiO_2 vs. Y diagram (after [44]), (**c**) ACF diagram (after [45]). FG—fractionated granite; OGT—ordinary granites of various types (i.e., I-, S-, and M-type granites).

Generally, S-type granites contain Al-rich minerals (e.g., cordierite, muscovite, garnet), have normative corundum content > 1%, and are strongly peraluminous (A/CNK > 1.1); I-type granites contain amphibole and pyroxene, with A/CNK < 1.1 [46]. P_2O_5 decreases with increasing fractionation in I-type granites, whereas it increases or shows no clear trend in S-type granites [12,47]. The Daning and Guiling plutons contain amphibole, with most samples showing A/CNK < 1.0 (Figure 6c). Their zircon saturation temperatures (Tzr: avg. 776 °C) are higher than those typical of S-type granites (Tzr < 750 °C) [48]. Moreover, most samples plot in the I-type fields on the SiO_2 vs. Y and ACF diagrams (Figure 10b,c), and the negative P_2O_5–SiO_2 correlation (Figure 5g) is consistent with an I-type affinity. These features collectively support the classification of both plutons as I-type granites.

5.2. Magma Source

I-type granites are generally attributed to four mechanisms: (1) fractional crystallization of mantle-derived mafic magmas with or without crustal contamination [48,49]; (2) partial melting of residual basaltic oceanic crust and sediments [50]; (3) partial melting of unmetamorphosed igneous rocks with or without mantle-derived magma addition [12,37]; and (4) mixing of crustal- and mantle-derived magmas [15,51].

Large-scale, contemporaneous mafic–ultramafic magmatism is lacking in eastern Guangxi (Figure 1b). The Daning and Guiling plutons have enriched isotopic compositions (ε_{Hf}(t): −4.6 to −1.2; ε_{Nd}(t): −13.6 to −5.0), with two-stage model ages (T_{2DM}: Hf = 1508–1702 Ma, Nd = 1584–2251 Ma), precluding a mantle-derived origin and indicating a crustal source. These isotopic features indicate that the granites were predominantly derived from a lower crustal source within the Paleoproterozoic basement (Figure 8a,b), rather than by partial melting of residual basaltic oceanic crust and sediments.

Previous studies and our data show that the Daning and Guiling granites have REE and incompatible element patterns (Figure 7) comparable to those of the Early Paleozoic granites in the Cathaysia Block. They also share similar patterns with the Precambrian basement lithologies (paragneisses, migmatites, schists, migmatized amphibolites, and minor pelitic granulites) of the eastern SCB [15]. In the source discrimination diagrams (Figure 11a,b), the samples predominantly plot within the mixing field between metaigneous and metagraywacke endmembers, and show close geochemical affinities with the Wuyi–Yunkai I-type granites [15]. Sr–Nd isotopic mixing models collectively suggest a mixed magma source (Figure 11c). However, the high viscosity of granitic magma limits efficient mixing [52], and thus evidence of crust–mantle mixing should be preserved in petrographic features. Indeed, the Daning and Guiling granites contain abundant mafic microgranular enclaves with K-feldspar phenocrysts (Figure 3c,e). This is supported by multiple lines of geochemical evidence: intermediate biotite MgO contents (avg. 11.55 wt.%), falling between crustal (<6 wt.%) and mantle (>15 wt.%) endmembers; whole-rock elevated

Rb/Sr ratios (avg. 2.50 vs. upper crust of 0.31), transitional Zr/Hf ratios (avg. 34.14, between crustal values of 33.0 and mantle values of 36.3), and high Tzr values (avg. 774 °C), comparable to those of the Fogang granite, which is considered to have formed by crust–mantle mixing. Moreover, our new U–Pb data, together with previous studies [15], confirm consistent zircon ages (Figure 4d) but a wide range of ε_{Hf}(t) values (−9.62 to −0.14), higher than those of Wuyi–Yunkai S-type granites (−19.72 to −2.2 [15,53]). The above results collectively point to a mixed crust–mantle source. This is further supported by Sr–Nd mixing models (Figure 11c), which indicate mantle input.

In fact, the Early Paleozoic granites in the SCB exhibit significant compositional heterogeneity [53,54]. However, whether this diversity reflects a heterogeneous crustal source [53] or crust–mantle magma mixing [3,5,51,54] remains controversial. As shown above, crust–mantle magma mixing played a key role in the genesis of the Daning and Guiling granites. Nevertheless, the two plutons show distinct differences in geochemical compositions and source characteristics. The Daning pluton has higher $Mg^{\#}$ (avg. 45.2) and lower Tzr (avg. 757 °C), with MMEs showing Nd isotopic compositions (ε_{Nd}(t): avg. −7.9; T_{2DM}: 1713–1914 Ma) similar to that of their host rocks (ε_{Nd}(t): −6.3; T_{2DM}: 1701 Ma). In contrast, the Guiling pluton exhibits a more complex signature, characterized by lower $Mg^{\#}$ (avg. 38.5), higher Tzr (avg. 791 °C), and F- and Cl-rich biotite (Figure 9b). Its MMEs show positive ε_{Nd}(t) (+3.43 to +3.58) and young T_{2DM} (911–923 Ma), distinct from the host rocks (ε_{Nd}(t): avg. −7.7; T_{2DM}: 1584–2251 Ma). Source discrimination diagrams and Sr–Nd mixing models (Figure 11c) further suggest that the Daning pluton is dominated by ~75% metaigneous and ~20% metasedimentary components, with limited mantle input (~5%). In comparison, the Guiling pluton appears to have a more complex source, with ~70% metagraywacke and metaigneous, ~20% metasedimentary, as well as ~10% mantle components.

Collectively, we propose that the source of the studied granites involved both a heterogeneous crustal component and magma mixing, while the Guiling pluton was derived from a more complex source with greater contributions of mantle-derived material, heat, and volatiles than the Daning pluton.

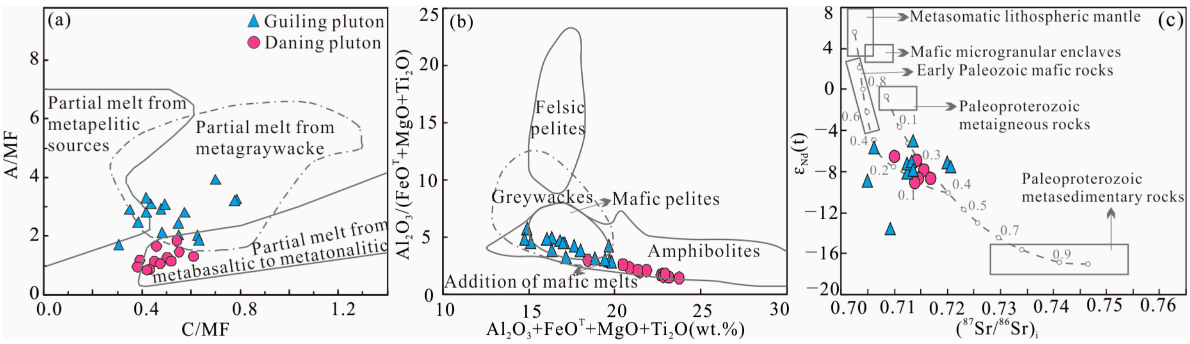

Figure 11. Source discrimination diagrams for the Daning and Guiling plutons. Whole-rock (**a**) C/MF vs. A/MF diagram (after [55]); (**b**) Al_2O_3 + FeO^T + MgO + Ti_2O vs. $Al_2O_3/(FeO^T + MgO + Ti_2O)$ diagram (after [56]); (**c**) $(^{87}Sr/^{86}Sr)_i$ vs. ε_{Nd}(t) diagram (after [15]). Data sources of Paleoproterozoic basement, metasomatic lithosphere mantle, Early Paleozoic mafic rocks, and mafic microgranular enclaves are from Tang et al. [15].

5.3. Magmatic Fractional Crystallization and Evolution

Previous work has shown that crustal partial melting or simple mixing between crustal and mantle melts cannot fully account for the elemental compositions of granitic rocks [15]. The Daning and Guiling granites are characterized by elevated SiO_2, low CaO and K/Rb ratios (Table S2), positive Rb–Th–U anomalies, pronounced Ba–Sr–Nb–Ti–P depletions, moderate Eu anomalies, and weak negative Zr anomalies (Figure 7a,b), suggesting significant fractional crystallization of their parental magmas. This is consistent with the negative correlations between SiO_2 and FeO^T, MgO, TiO_2, MnO, Al_2O_3, CaO, and P_2O_5 (Figure 5a–g).

Plagioclase fractionation is supported by Sr depletion, moderate Eu anomalies (Figure 12a,b), and CaO–SiO_2 anticorrelation (Figure 5f). The increase in K_2O with SiO_2 (Figure 5i) and pronounced Ba depletion may be related to biotite fractionation (Figure 12b). The negative Nb and Ti anomalies reflect the removal of Ti-bearing phases (e.g., rutile, ilmenite, titanite; Figure 12c), whereas the P_2O_5–SiO_2 trend (Figure 5g) and low P_2O_5 contents indicate apatite fractionation. However, a few samples exhibit relatively low Tzr values (637–702 °C) with weak negative Zr anomalies, which may be related to the extreme oversaturation of zircon at low temperatures, facilitating its crystallization [57]. Overall, although both plutons mainly underwent fractional crystallization, their fractionation assemblages differ markedly: the Daning pluton is dominated by magnetite + ilmenite + biotite fractionation, whereas the Guiling pluton is characterized by plagioclase + ilmenite fractionation.

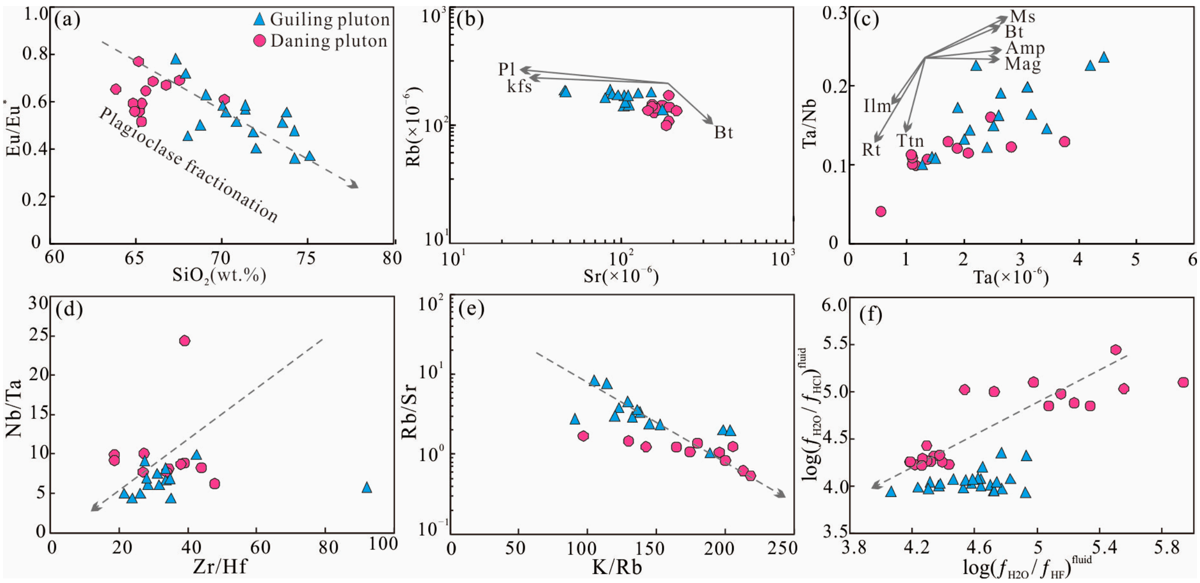

Figure 12. (**a**) SiO_2 vs. Eu/Eu* diagram, (**b**) Sr vs. Rb diagram, (**c**) Ta vs. Ta/Nb diagram, (**d**) Zr/Hf vs. Nb/Ta diagram, (**e**) Rb/Sr vs. SiO_2 diagram, and (**f**) $\log(f_{H2O}/f_{HF})^{fluid}$ vs. $\log(f_{H2O}/f_{HCl})^{fluid}$ diagram for the Daning and Guiling plutons. Bt: biotite; Ms: muscovite; Mag: magnetite; Ilm: ilmenite; Rt: rutile; Ttn: titanite; Amp: amphibole.

Additionally, comparative analysis shows that the Guiling pluton is more evolved than the Daning pluton, as indicated by its higher SiO_2, Al_2O_3, Na_2O, and K_2O contents, more ferroan biotite composition (Figure 9a), relatively strong negative Eu anomaly (Figure 7a), lower ratios of K/Rb, Nb/Ta, and Zr/Hf, and higher Rb/Sr ratios and differentiation indices (Figure 12d,e). It also falls within the fractionated granite (FG) field (Figure 10a) and exhibits higher zircon saturation temperatures. Biotite compositions further reveal elevated volatile (F and Cl) contents with lower $\log(f_{H2O}/f_{HF})^{fluid}$, and higher $\log(f_{H2O}/f_{HCl})^{fluid}$ values in the Guiling pluton (Figure 12f), with lower biotite solidification pressures, suggesting reduced melt viscosity, shallower emplacement and F- and Cl-rich fluid exsolution in a highly fractionated system.

5.4. Tectonic Setting

Granite is a major lithological component of continental crust, and its geochemical composition provides robust constraints on contemporaneous tectonic settings. It is widely accepted that the South China Block experienced an intracontinental orogenic process during the Caledonian period, with the related granites recording a complete cycle of crustal thickening, peak anatexis, and subsequent extensional collapse [58]. Regional geological evidence shows that ductile shearing associated with crustal shortening occurred at ca. 450–435 Ma, whereas granulite- and amphibolite-facies metamorphism in the Cathaysia Block peaked at ca. 460–440 Ma [59]. Moreover, the South China Block is marked by the development of Devonian–Carboniferous graben systems, Devonian strike-slip pull-apart basins, extensive Devonian passive-margin deposits [16], and the emplacement of Early Devonian (414–401 Ma) A-type granites and diabases [60], which are interpreted as indicators of a post-orogenic extensional regime. Collectively, these tectono-sedimentary–magmatic records imply that the South China Block had already entered the post-orogenic extensional stage by the Early Devonian (<420 Ma).

The Daning and Guiling plutons exhibit massive fabrics and lack syn-collisional ductile deformation structures. Their emplacement ages of 440–425 Ma (Figure 4d) suggest that they were emplaced during the transitional period from compression to extension. On the tectonic discrimination diagram (Figure 13), all samples plot in the post-collisional field, straddling the boundary between syn-collisional and within-plate granite fields, and display a clockwise evolutionary trend, indicating a tectonic transition from syn-collisional to post-collisional (within-plate) settings. We therefore conclude that the Daning and Guiling granites were formed in an intracontinental orogenic setting during the switch from crustal compression to extensional relaxation. Relative to the Daning pluton, the Guiling pluton likely formed in a more pronounced extensional setting.

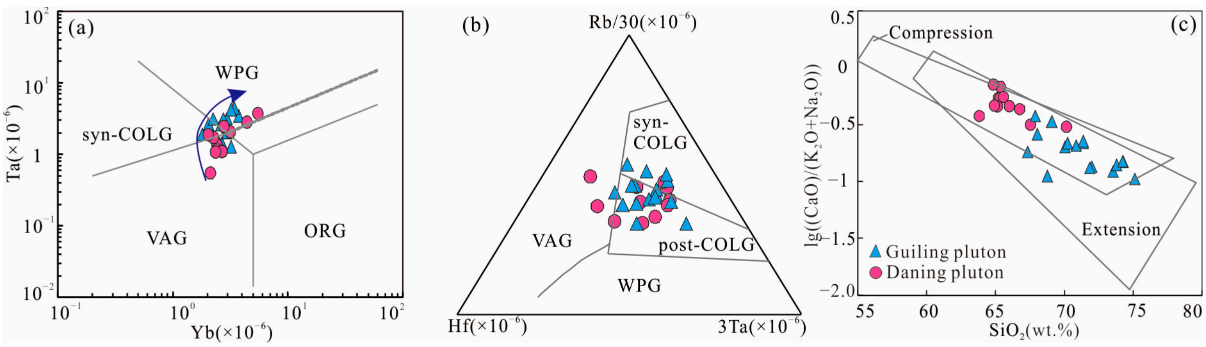

Figure 13. The tectonic discrimination diagrams (**a**) Yb vs. Ta* diagram (after [61]), (**b**) Rb/30 vs. Hf vs. 3Ta diagram (after [62]), and (**c**) SiO_2 vs. lg((CaO)/(K_2O + Na_2O)) diagram (after [63]) for the Daning and Guiling plutons. OGR: ocean ridge granites; WPG: within-plate granites; VAG: volcanic arc granites; syn-COLG: Syn-collision granites; post-COLG: post-collision granites.

5.5. Magmatic Controls on Molybdenum Mineralization

(1) Magmatic oxygen fugacity controls

Mo behavior is redox-sensitive, and its speciation is controlled by magmatic oxygen fugacity (fO_2) [64]. Under high fO_2, Mo exists as Mo^{6+}, forming soluble molybdates that can be transported by fluids. High-fO_{22} melts extract Mo from Mo-rich sediments, enhance Mo mobility, and inhibit early Mo sulfide precipitation; thus, most Mo-related magmas have high fO_2. Under reducing conditions, Mo exists as Mo^{4+}, forming molybdenite or being trapped by early minerals, limiting Mo availability for fluids. Low fO_2 reduces Mo mobility and suppresses redox-driven isotope fractionation, hindering Mo mineralization [8]. Our biotite data (Figure 9f) show that the Guiling and Daning plutons have similar fO_2 values (avg. −17.47 vs. −17.58, respectively), both near NNO, indicating moderate fO_2, where Mo exists as Mo^{6+} and can be enriched in residual melts. Thus, oxygen fugacity is not the key factor controlling the contrasting Mo fertility of the two plutons.

(2) Magmatic fractional crystallization and evolution controls

Mo-mineralized granites are often highly fractionated, and the continuous accumulation of Mo in the residual melt during intense magmatic fractional crystallization is a critical factor for its exceptional enrichment and mineralization [7,8]. The partitioning behavior of molybdenum (Mo) varies considerably among major rock-forming and accessory minerals. Mo is moderately to weakly incompatible in magnetite (partition coefficient K_D = 0.21–0.52) [65] and ilmenite (K_D = 0.22–0.42) [66], so fractionation of Fe–Ti oxides can effectively remove Mo from the melt. Biotite (K_D = 0.29) also sequesters Mo [67], further contributing to Mo depletion. In contrast, Mo is strongly incompatible in plagioclase [68], whose fractionation does not significantly reduce Mo in the residual magma. Amphibole (K_D = 0.11–0.25) crystallization consumes Cl [69], limiting Cl availability for late-stage Mo mobilization. Although ilmenite fractionation occurred in both plutons, the Daning pluton contains relatively more amphibole and biotite, where magnetite and biotite fractionation may have promoted Mo removal, and amphibole crystallization likely consumed Cl, both potentially hindering Mo enrichment. In contrast, the Guiling pluton shows plagioclase-dominated fractionation and relatively less amphibole and biotite, which would have favored Cl retention in the residual melt and thus may have enhanced its Mo mineralization potential. Notably, experimental and geochemical studies have suggested that increasing F contents may reduce melt density and viscosity [70], promote crystal settling, lower the magma solidus temperature, and prolong magma evolution [8], all of which could favor the continuous enrichment of ore-forming metals in the residual melt. Moreover, high-temperature and high-pressure experiments, combined with molecular dynamics simulations, have demonstrated that Cl can form stable Mo complexes (e.g., $MoO_2(OH)Cl$ and $NaMoO_3Cl$) under magmatic–hydrothermal conditions, and that the initial Cl concentration in the melt largely controls the efficiency of Mo extraction by fluids [71]. As discussed above, compared to the Daning pluton, the Guiling pluton is more volatile-rich (F, Cl) and shows higher degrees of fractionation, collectively supporting its greater magmatic–hydrothermal potential. Therefore, the F- and Cl-rich fluids in the Guiling pluton would have facilitated efficient Mo extraction from the melt, sustained its transport in the hydrothermal system, and ultimately promoted its precipitation and enrichment at favorable structural sites.

(3) Magma source and tectonic structure controls

The scale of quartz vein-type Mo deposits is controlled by source characteristics [5]. Mo abundance is highest in the upper crust (~1.5×10^{-6}), intermediate in the lower crust (~0.6×10^{-6}), and lowest in the mantle (~0.05×10^{-6}) [36,72]. A purely crustal source can supply Mo metals, but limited thermal input may restrict hydrothermal system scale (e.g., the small Majiawa deposit in Xiaoqinling) [8,73]. Conversely, a purely mantle source has insufficient Mo to support mineralization independently. For example, the Jigongcun deposits in Tibet are derived from delaminated lower crust rather than direct mantle supply [74]. Thus, a crust–mantle mixed source, combining crustal Mo with mantle-derived heat and volatiles [6], may be more favorable for medium- to large-scale deposits (e.g., Qianfanling [75]). In this crust–mantle mixed-source framework, upwelling mantle-derived materials provided both the high heat flow required for crustal remelting and abundant volatiles [76]. Among these, F and Cl help lower crustal melting temperatures, promote remelting, and form efficient Mo complexes in hydrothermal fluids [71]. The synergistic effects of these factors facilitated Mo release from the source and its continuous enrichment in residual melts. As discussed above, the spatially adjacent Guiling and Daning plutons are both I-type granites but differ significantly in magma sources. The Guiling pluton has higher Mo content (avg. 1.4×10^{-6}), higher Tzr (avg. 791 °C), and higher F and Cl contents (Figure 9a) than the Daning pluton (Mo: avg. 0.6×10^{-6}; Tzr: avg. 757 °C). The source of the studied granites involved both crustal heterogeneity and magma mixing, whereas the Guiling pluton was derived from a more complex source with greater contributions of mantle-derived material, heat, and volatiles than the Daning pluton. These differences suggest that mantle input facilitated Mo mineralization not by directly contributing metal, but by supplying heat to power crustal melting and volatiles (F, Cl) to sustain prolonged magmatic differentiation, a process crucial for Mo enrichment.

This contrast in mantle contribution can be explained by their distinct tectonic settings during emplacement. The Daning and Guiling granites (440–425 Ma; Figure 4d) were emplaced during the transition from crustal compression to extensional relaxation within an intracontinental orogenic setting. Compared to the earlier Daning pluton, the younger Guiling pluton formed under a more pronounced extensional regime, when post-orogenic collapse of the thickened lithosphere induced crustal thinning and asthenospheric upwelling [51]. Mantle-derived heat triggered lower-crustal partial melting, producing crust–mantle hybrid magmas [15], which ascended along pre-existing conduits to form I-type granites [16]. This more pronounced extensional setting thus enabled greater inputs of mantle-derived heat and volatiles into the Guiling magmatic system, creating conditions favorable for Mo enrichment.

Notably, the Guiling pluton is situated between the NE-trending Longwu (LW) and Yingyangguan (YYG) Caledonian ductile shear zones (Figure 2), and the Baishiding Mo deposit is located at the southwestern end of the LW ductile shear zone. Although no contemporaneous Mo mineralization has been recognized along the YYG ductile shear zone, biotite mineral chemistry data from sample 13120 of the Daning pluton (proximal to the southwestern segment of YYG ductile shear zone) are broadly comparable to those of the Guiling pluton in terms of Cl content, log(Cl/OH) ratio, crystallization temperature, and oxygen fugacity (Table S5; Figure 9). This observation, together with the spatial proximity to the ductile shear zone, may have implications for Mo prospecting in the southwestern segment of the YYG ductile shear zone. Regionally, it is plausible that the Caledonian ductile shear zones functioned as both structural controls and fluid conduits, consistent with the widely recognized view that hydrothermal vein-type mineralization requires favorable chemical conditions and appropriate structural traps for fluid precipitation and metal accumulation [77,78]. Thus, the similarity in physicochemical conditions between the Daning pluton and the mineralized Guiling pluton suggests that the southwestern segment of the YYG ductile shear zone between the Daning and Guiling plutons could be a prospective target for Mo prospecting.

In summary, the contrasting Mo fertility of the Caledonian granites in eastern Guangxi was governed by both magmatic and structural factors. Mantle-derived heat and volatiles promoted crustal Mo enrichment by sustaining prolonged differentiation, and ductile shear zones provided the structural pathways that focused ore-forming fluids.

6. Conclusions

(1) The Guiling monzogranite (Mo-mineralized) and Daning granodiorite (Mo-barren) in eastern Guangxi are both I-type granites, but the Guiling pluton is younger (~425 Ma) and more evolved than the Daning pluton (~440 Ma).

(2) The Daning and Guiling plutons share a mixed crust–mantle source and were both emplaced during the transition from compression to extension, but the more pro-

nounced extension facilitated greater inputs of mantle-derived heat and volatiles into the Guiling pluton, favoring Mo enrichment.

(3) The contrasting Mo fertility between the two plutons reflects the interplay of magmatic and structural factors. Crust–mantle source mixing, high degrees of fractionation, and volatile enrichment promoted Mo concentration, whereas ductile shear zones would have served as conduits that focused mineralization.

(4) The southwestern segment of the Yingyangguan (YYG) ductile shear zone between the Daning and Guiling plutons could be a prospective target for Mo prospecting.

Supplementary Materials: The following supporting information can be downloaded at: https://www.mdpi.com/article/10.3390/min16070739/s1, Table S1: Zrcon U–Pb results from the Caledonian granites in eastern Guangxi; Table S2: Whole-rock results from the Caledonian granites in eastern Guangxi; Table S3: Zrcon Hf Isotope results from the Caledonian granites in eastern Guangxi; Table S4: Whole-rock Nd Isotope results from the Caledonian granites in eastern Guangxi; Table S5: EPMA results for biotite from the Caledonian granites in eastern Guangxi (wt.%).

Author Contributions: Conceptualization, L.M. and Y.L.; Methodology, L.M.; Formal Analysis, G.F. and Z.J.; Investigation, L.M., Y.L., Z.J. and E.W.; Resources, Y.L.; Data Curation, L.M. and L.Q.; Writing—Original Draft Preparation, L.M.; Writing—Review and Editing, Y.L. and B.W.M.; Supervision, Y.L.; Project Administration, Y.L.; Funding Acquisition, Y.L. and G.F.; All authors have read and agreed to the published version of the manuscript.

Funding: This research was funded by the Natural Science Foundation of Guangxi, grant number 2026GXNSFAA00641205; the Guangxi Science and Technology Program, grant number Guike LT2600640017; the National Natural Science Foundation of China, grant number 42372099; and the Start-Up Research Grant of Guilin University of Technology, grant number RD2600000936.

Data Availability Statement: The original data presented in the study are included in the article; further inquiries can be directed to the corresponding author.

Acknowledgments: We are grateful to the editors and anonymous reviewers for their constructive comments.

Conflicts of Interest: The authors declare no conflicts of interest.

References

1. Mao, J.W.; Liu, P.; Goldfarb, R.J.; Goryachev, N.A.; Pirajno, F.; Zheng, W.; Zhou, M.F.; Zhao, C.; Xie, G.Q.; Yuan, S.D.; et al. Cretaceous large-scale metal accumulation triggered by post-subductional large-scale extension, East Asia. *Ore Geol. Rev.* **2021**, *136*, 104270.
2. Dang, Y.; Chen, M.H.; Mao, J.W.; Fu, B. Weakly fractionated I-type granitoids and their relationship to tungsten mineralization: A case study from the Early Paleozoic Shangmushui deposit, Dayaoshan area, South China. *Ore Geol. Rev.* **2020**, *117*, 103281. [CrossRef]
3. Huang, F.; Wang, D.H.; Wang, C.H.; Chen, Z.H.; Yuan, Z.X.; Liu, X.X. Relationship between Caledonian granitoids and large-scale mineralization in South China. *Acta Geol. Sin.* **2014**, *88*, 2296–2314. (In Chinese with English abstract)
4. Jiang, X.Z.; Kang, Z.Q.; Xu, J.F.; Feng, Z.H.; Pang, C.J.; Fang, G.C.; Wu, J.C.; Xiong, S.Q. Early Paleozoic granodioritic plutons in the Shedong W-Mo ore district, Guangxi, southern China: Products of re-melting of middle Proterozoic crust due to magma underplating. *J. Asian Earth Sci.* **2017**, *141*, 59–73.
5. Yuan, Y.; An, F.; Chen, B. A review of the research status of geological and geochemical characteristics of quartz vein-type molybdenum deposits. *Chin. J. Geol.* **2020**, *55*, 598–614. (In Chinese with English abstract)
6. Yang, F.; Ge, X.Y.; Qin, Z.Y.; Xu, L.F.; Wang, L.Y.; Yang, L.K.; Su, H. Biotite unravels F-driven Mo mineralization and magmatic-hydrothermal evolution in the Chaijiaqou porphyry deposit, North China. *J. Geochem. Explor.* **2026**, *288*, 108123.
7. Xiao, B.; Li, Q.G.; Liu, S.W.; Wang, Z.Q.; Yang, P.T.; Chen, J.L.; Xu, X.Y. Highly fractionated Late Triassic I-type granites and related molybdenum mineralization in the Qinling orogenic belt: Geochemical and U–Pb–Hf and Re–Os isotope constraints. *Ore Geol. Rev.* **2014**, *56*, 220–233. [CrossRef]
8. Cao, C.; Shen, P. Advances and problems in study of porphyry molybdenum deposits. *Geol. Rev.* **2018**, *64*, 477–497. (In Chinese with English abstract)

9. Huang, W.T.; Wu, J.; Zhang, J.; Liang, H.Y.; Qiu, X.L. Geochemistry and Hf-Nd isotope characteristics and forming processes of the Yuntoujie granites associated with W-Mo deposit, Guangxi, South China. *Ore Geol. Rev.* **2017**, *81*, 953–964. [CrossRef]
10. Ma, X.H.; Wang, H.H.; Lehmann, B.; Guo, C.L.; Mao, J.W. Control of magmatic halogen composition and redox state on the zonation of metal mineralization across active continental margins: Perspectives from the world-class South China metallogenic province. *Chem. Geol.* **2024**, *669*, 122363. [CrossRef]
11. Jiang, H.; Jiang, S.Y. Petrogenesis of early Silurian I-type granitoids in the Nanling domain, South China: Implications for the evolution of the Wuyi-Yunkai orogen. *J. Asian Earth Sci.* **2026**, *297*, 106917. [CrossRef]
12. Zhong, J.; Chen, Y.J.; Pirajno, F. Geology, geochemistry and tectonic settings of the molybdenum deposits in South China: A review. *Ore Geol. Rev.* **2017**, *81*, 829–855. [CrossRef]
13. Li, X.F.; Feng, Z.H.; Li, R.S.; Tang, Z.H.; Qu, W.J.; Li, J.C. Silurian Mo mineralization at Baishiding molybdenum deposit in northern Guangxi: Constraints from zircon SHRIMP U-Pb and molybdenite Re-Os ages. *Miner. Depos.* **2009**, *28*, 403–412. (In Chinese with English abstract)
14. Yan, C.L.; Shu, L.S.; Faure, M.; Chen, Y.; Li, C. Early Paleozoic intracontinental orogeny in the Yunkai domain, South China Block: New insights from field observations, zircon U-Pb geochronological and geochemical investigations. *Lithos* **2017**, *268–271*, 320–333. [CrossRef]
15. Tang, Y.L.; Shi, Y.; Hu, X.M.; Liu, X.J.; Huang, C.W. Petrogenesis of Early Paleozoic I-type granitoids in the Wuyi-Yunkai Orogen, South China: Implications for the tectono-magmatic evolution of the Cathaysia Block. *J. Asian Earth Sci.* **2021**, *220*, 104906. [CrossRef]
16. Liu, Y.Z. *Caledonian Granites in the Western Nanling Range: Structural Patterns, Spatio-Temporal Magmatic Evolution, and Tectonic Implications*; Guilin University of Technology: Guilin, China, 2025; pp. 1–261. (In Chinese with English abstract)
17. Chen, M.H.; Mo, C.S.; Huang, Z.Z.; Li, B.; Huang, H.W. Zircon LA-ICP-MS U-Pb ages of granitoid rocks and molybdenite Re-Os age of Shedong W-Mo deposit in Cangwu County of Guangxi and its geological significance. *Miner. Depos.* **2011**, *30*, 963–978. (In Chinese with English abstract)
18. Chen, M.H.; Guo, Y.Q.; Liang, B.; Huang, H.W. Emplaced and metallogenetic ages of Wujie tungsten and molybdenum occurrence and geochemical characteristics of granodiorite in Cangwu. *J. Guilin Univ. Technol.* **2012**, *32*, 1–13. (In Chinese with English abstract)
19. Jackson, S.E.; Pearson, N.J.; Griffin, W.L.; Belousova, E.A. The application of laser ablation-inductively coupled plasma-mass spectrometry to In Situ U-Pb zircon geochronology. *Chem. Geol.* **2004**, *211*, 47–69. [CrossRef]
20. Sláma, J.; Košler, J.; Condon, D.J.; Crowley, J.L.; Gerdes, A.; Hanchar, J.M.; Horstwood, M.S.A.; Morris, G.A.; Nasdala, L.; Norberg, N.; et al. Plešovice zircon—A new natural reference material for U-Pb and Hf isotopic microanalysis. *Chem. Geol.* **2008**, *249*, 1–35. [CrossRef]
21. Andersen, T. Correction of common lead in U-Pb analyses that do not report 204Pb. *Chem. Geol.* **2002**, *192*, 59–79. [CrossRef]
22. Huang, F.; Xu, J.F.; Chen, J.L.; Wu, J.B.; Zeng, Y.C.; Xiong, Q.W.; Chen, X.F.; Yu, H.X. Two Cenozoic tectonic events of N-S and E-W extension in the Lhasa Terrane: Evidence from geology and geochronology. *Lithos* **2016**, *245*, 118–132. [CrossRef]
23. Lin, W.W.; Peng, L.J. The estimation of Fe^{3+} and Fe^{2+} contents in amphibole and biotite from EMPA data. *J. Chang. Univ. Earth Sci.* **1994**, *24*, 155–162. (In Chinese with English abstract)
24. Uchida, E.; Endo, S.; Makino, M. Relationship between solidification depth of granitic rocks and formation of hydrothermal ore deposits. *Resour. Geol.* **2007**, *57*, 47–56. [CrossRef]
25. Munoz, J.L. F-OH and Cl-OH exchange in micas with applications to hydrothermal ore deposits. In *Micas*; Reviews in Mineralogy; Bailey, S.W., Ed.; Mineralogical Society of America: Chantilly, VA, USA, 1984; Volume 13, pp. 469–494.
26. Zhu, C.; Sverjensky, D.A. F-Cl-OH partitioning between biotite and apatite. *Geochim. Cosmochim. Acta* **1992**, *56*, 3435–3467. [CrossRef]
27. Mo, L.; Liu, Y.Z.; Fang, G.C.; Bai, Y.M.; Zheng, G.F.; Wu, J.; Wu, X.J. Comparison of mineral chemistry of biotite between Caledonian Yuechengling and western Dupangling granites in northern Guangxi and its implication for petrogenesis and mineralization. *J. Guilin Univ. Technol.* **2024**, *44*, 175–193. (In Chinese with English abstract)
28. Cheng, S.B.; Fu, J.M.; Xu, D.M.; Chen, X.Q.; Ma, L.Y.; Wang, X.D.; Pang, Y.C. Zircon SHRIMP U-Pb dating and geochemical characteristics of Daning batholith in northeast Guangxi. *Geol. China* **2009**, *36*, 1278–1288, In Chinese with English abstract.
29. Yuan, A.P. *Study on the Emplacement Mechanism of Daning Granite Pluton in Eastern Guangxi*; Guilin University of Technology: Guilin, China, 2005; pp. 1–72. (In Chinese with English abstract)
30. Feng, Z.H. *Emplacement Process and Structural Analysis of Guposhan-Huashan Granitic Pluton, Guangxi*; Central South University: Changsha, China, 2003; pp. 1–158. (In Chinese with English abstract)
31. Wang, L. *Chronology, Petrology, Geochemistry and Petrogenesis of Daning Granitic Pluton and Its Mafic Enclaves, Northeast Guangxi*; Chinese Academy of Geological Sciences: Beijing, China, 2014; pp. 1–81. (In Chinese with English abstract)
32. Guangxi Institute of Geological Survey. *Regional Geological Survey Report of Hezhou Sheet (1:250,000)*; Guangxi Institute of Geological Survey: Beihai, China, 2005; pp. 1–397. (In Chinese with English abstract)

33. Wei, C.X. *Petrogenesis and Tectonic Geological Setting of Caledonian Granitoids in Northeast Guangxi*; China University of Geosciences: Beijing, China, 2016; pp. 1–74. (In Chinese with English abstract)
34. Middlemost, E.A.K. Naming materials in the magma igneous rock system. *Earth-Sci. Rev.* **1994**, *37*, 215–224. [CrossRef]
35. Peccerillo, R.; Taylor, S.R. Geochemistry of Eocene calc-alkaline volcanic rocks from the Kastamonu area, Northern Turkey. *Contrib. Mineral. Petrol.* **1976**, *58*, 63–81. [CrossRef]
36. Sun, S.S.; McDonough, W.F. Chemical and isotopic systematics of oceanic basalts: Implications for mantle composition and processes. *Geol. Soc. Lond. Spec. Publ.* **1989**, *42*, 313–345. [CrossRef]
37. Kong, H.; Wu, J.H.; Li, H.; Chen, S.F.; Liu, B.; Wang, G. Early Paleozoic tectonic evolution of the South China Block: Constraints from geochemistry and geochronology of granitoids in Hunan Province. *Lithos* **2021**, *380–381*, 105891. [CrossRef]
38. Foster, M.D. Interpretation of the composition of trioctahedral micas. *Geol. Surv. Prof. Pap.* **1960**, *354-B*, 11–49.
39. Henry, D.J.; Guidotti, C.V.; Thomson, J.A. The Ti-saturation surface for low-to-medium pressure metapelitic biotites: Implications for geothermometry and Ti-substitution mechanisms. *Am. Mineral.* **2005**, *90*, 316–328. [CrossRef]
40. Wones, D.R. Significance of the assemblage titanite + magnetite + quartz in granitic rocks. *Am. Mineral.* **1989**, *74*, 744–749.
41. Pitcher, W.S. *The Nature and Origin of Granite*; Blackie Academic and Professional: London, UK, 1993; pp. 1–321.
42. Whalen, J.B.; Currie, K.L.; Chappell, B.W. A-type granites: Geochemical characteristics, discrimination and petrogenesis. *Contrib. Mineral. Petrol.* **1987**, *95*, 407–419. [CrossRef]
43. Wu, F.Y.; Li, X.H.; Yang, J.H.; Zheng, Y.F. Discussions on the petrogenesis of granites. *Acta Petrol. Sin.* **2007**, *23*, 1217–1238. (In Chinese with English abstract)
44. Collins, W.J.; Beams, S.D.; White, A.J.R.; Chappell, B.W. Nature and origin of A-type granites with particular reference to southeastern Australia. *Contrib. Mineral. Petrol.* **1982**, *80*, 189–200. [CrossRef]
45. Hine, R.; Williams, I.S.; Chappell, B.W.; White, A.J.R. Contrasts between I- and S-type granitoids of the Kosciusko Batholith. *J. Geol. Soc. Aust.* **1978**, *25*, 219–234. [CrossRef]
46. Chappell, B.W. Aluminium saturation in I- and S-type granites and the characterization of fractionated haplogranites. *Lithos* **1999**, *46*, 535–551. [CrossRef]
47. Chappell, B.W.; White, A.J.R.; Williams, I.S.; Wyborn, D. Low- and high-temperature granites. *Trans. R. Soc. Edinb. Earth Sci.* **2004**, *95*, 125–140. [CrossRef]
48. Soesoo, A. Fractional crystallization of mantle-derived melts as a mechanism for some I-type granite petrogenesis: An example from Lachlan Fold Belt, Australia. *J. Geol. Soc.* **2000**, *157*, 135–149. [CrossRef]
49. Xia, Y.; Xu, X.S.; Zou, H.B.; Liu, L. Early Paleozoic crust-mantle interaction and lithosphere delamination in South China Block: Evidence from geochronology, geochemistry, and Sr-Nd-Hf isotopes of granites. *Lithos* **2014**, *184–187*, 416–435. [CrossRef]
50. Castro, A.; Gerya, T.; García-Casco, A.; Fernández, C. Melting relations of MORB-sediment mélanges in underplated mantle wedge plumes: Implications for the origin of Cordilleran-type batholiths. *J. Petrol.* **2010**, *51*, 1267–1295. [CrossRef]
51. Xie, Y.X.; Ma, L.Y.; Zhao, G.C.; Xie, C.F.; Han, Y.G.; Li, J.H.; Liu, Q.; Yao, J.L.; Zhang, Y.Y.; Lu, Y.F. Origin of the Heping granodiorite pluton: Implications for syn-convergent extension and asthenosphere upwelling accompanying the early Paleozoic orogeny in South China. *Gondwana Res.* **2020**, *85*, 149–168. [CrossRef]
52. Sparks, R.S.J.; Marshall, L.A. Thermal and mechanical constraints on mixing between mafic and silicic magmas. *J. Volcanol. Geotherm. Res.* **1986**, *29*, 99–124. [CrossRef]
53. Wang, Y.J.; Zhang, A.M.; Fan, W.M.; Zhao, G.C.; Zhang, G.W.; Zhang, Y.Z.; Zhang, F.F.; Li, S.Z. Kwangsian crustal anatexis within the eastern South China Block: Geochemical, zircon U-Pb geochronological and Hf isotopic fingerprints from the gneissoid granites of Wugong and Wuyi-Yunkai Domains. *Lithos* **2011**, *127*, 239–260. [CrossRef]
54. Zhang, Q.; Jiang, Y.H.; Wang, G.C.; Liu, Z.; Ni, C.Y.; Qing, L. Origin of Silurian gabbros and I–type granites in Central Fujian, SE China: Implications for the evolution of the Early Paleozoic orogen of South China. *Lithos* **2015**, *216*, 285–329. [CrossRef]
55. Altherr, R.; Holl, A.; Hegner, E.; Langer, C.; Kreuzer, H. High-potassium, calc-alkaline I-type plutonism in the European Variscides: Northern Vosges (France) and northern Schwarzwald (Germany). *Lithos* **2000**, *50*, 51–73. [CrossRef]
56. Patiño Douce, A.E. What do experiments tell us about relative contributions of crust and mantle to the origin of granitic magmas? In *Understanding Granites: Integrating New and Classical Techniques*; Special Publications; Castro, A., Fernandez, C., Vigneresse, J.L., Eds.; Geological Society of London: London, UK, 1999; Volume 168, pp. 55–75.
57. Crisp, L.J.; Berry, A.J. Correction to: A new model for zircon saturation in silicate melts. *Contrib. Mineral. Petrol.* **2024**, *179*, 75. [CrossRef]
58. Shu, L.S.; Wang, B.; Cawood, P.A.; Santosh, M.; Xu, Z.Q. Early Paleozoic and Early Mesozoic intraplate tectonic and magmatic events in the Cathaysia Block, South China. *Tectonics* **2015**, *34*, 1600–1621. [CrossRef]
59. Xia, Y.F.; Wang, L.J.; Rayner, N.; Lin, S.F.; Xiao, W.J.; Yin, C.Q.; Qian, J.H.; Liu, H.; Zhao, X.L. Metamorphic P-T-t evolution deciphered from episodic monazite growth in granulites of the Chencai Complex and implications for the Early Paleozoic Orogeny, West Cathaysia terrane, South China. *Geol. Soc. Lond. Spec. Publ.* **2024**, *542*, 643–663.

60. Xin, Y.; Li, J.; Ratschbacher, L.; Zhao, G.; Zhang, Y.; Dong, S.; Xia, X.P.; Yu, Y. Early Devonian (415–400 Ma) A-type granitoids and diabases in the Wuyishan, eastern Cathaysia: A signal of crustal extension coeval with the separation of South China from Gondwana. *Geol. Soc. Am. Bull.* **2020**, *132*, 2295–2317. [CrossRef]
61. Pearce, J. Sources and Settings of Granitic Rocks. *Episodes* **1996**, *19*, 120–125. [CrossRef]
62. Harris, N.B.; Pearce, J.A.; Tindle, A.G. Geochemical characteristics of collision-zone magmatism. *Geol. Soc. Lond. Spec. Publ.* **1986**, *19*, 67–81. [CrossRef]
63. Brown, G.C. Calc-alkaline intrusive rocks: Their diversity and relation to volcanic arcs. In *Andes-Orogenic Andes and Related Rocks*; Thorpe, S., Ed.; John Wiley and Sons: New York, NY, USA, 1982; pp. 437–464.
64. Rozenbaks, P.; Brenan, J.M. Redox-sensitive partitioning of vanadium and other heterovalent elements between apatite and biotite in high silica magmas. *Geochim. Cosmochim. Acta* **2025**, *402*, 291–315. [CrossRef]
65. Tacker, R.C.; Candela, P.A. Partitioning of molybdenum between magnetite and melt; a preliminary experimental study of partitioning of ore metals between silicic magmas and crystalline phases. *Econ. Geol.* **1987**, *82*, 1827–1838. [CrossRef]
66. Candela, P.A.; Bouton, S.L. The influence of oxygen fugacity on tungsten and molybdenum partitioning between silicate melts and ilmenite. *Econ. Geol.* **1990**, *85*, 633–640. [CrossRef]
67. Were, P.; Keppler, H. Trace element fractionation between biotite, allanite, and granitic melt. *Contrib. Mineral. Petrol.* **2021**, *176*, 74. [CrossRef]
68. Dunn, T.; Sen, C. Mineral/matrix partition coefficients for orthopyroxene, plagioclase, and olivine in basaltic to andesitic systems: A combined analytical and experimental study. *Geochim. Cosmochim. Acta* **1994**, *58*, 717–733. [CrossRef]
69. Dawson, H.G.; Carpenter, P.K.; Krawczynski, M.J. Amphibole–silicate melt halogen partition coefficients: Cryptic amphibole fractionation and chlorine to fluorine ratios in arc magmas. *Contrib. Mineral. Petrol.* **2025**, *180*, 60. [CrossRef]
70. Dingwell, D.B.; Knoche, R.; Webb, S.L. The effect of F on the density of haplogranite melt. *Am. Mineral.* **1993**, *78*, 325–330.
71. Guan, Q.S.; Mei, Y.; Liu, W.H.; Brugger, J. Different metal coordination in sub- and super-critical fluids: Do molybdenum(IV) chloride complexes contribute to mass transfer in magmatic systems? *Geochim. Cosmochim. Acta.* **2023**, *354*, 240–251. [CrossRef]
72. Rudnick, R.L.; Gao, S. Composition of the continental crust. In *Treatise on Geochemistry, Volume 3: The Crust*; Rudnick, R.L., Ed.; Elsevier: Amsterdam, The Netherlands, 2003; pp. 1–64.
73. Wang, Y.T.; Ye, H.S.; Ye, A.W.; Li, Y.G.; Shuai, Y.; Zhang, C.Q.; Dai, J.Z. Re-Os age of molybdenum from the Majiawa Au-Mo deposit of quartz vein type in the north margin of the Xiaoqinling gold area and its implication for metallogeny. *Earth Sci. Front.* **2010**, *17*, 140–145. (In Chinese with English abstract)
74. Zhang, Z.; Li, G.M.; Yang, Y.; Zhang, L.K.; Lian, T.R.; Huang, Y.; Li, Y.B.; Dong, S.L. Genesis of the Jigongcun Re-rich quartz vein-type Mo deposit, southern Tibet: Constraints from mineralogy, fluid inclusions, geochronology, H-O-S isotopes, and in situ trace element compositions of molybdenite. *Ore Geol. Rev.* **2021**, *132*, 104069. [CrossRef]
75. Gao, Y.; Mao, J.W.; Ye, H.S.; Li, Y.F. Origins of ore-forming fluid and material of the quartz-vein type Mo deposits in the East Qinling-Dabie molybdenum belt: A case study of the Qianfanling Mo deposit. *J. Geochem. Explor.* **2018**, *185*, 52–63. [CrossRef]
76. Kendrick, M.A.; Jackson, M.G.; Kent, A.J.R.; Hauri, E.H.; Wallace, P.J.; Woodhead, J. Contrasting behaviours of CO_2, S, H_2O and halogens (F, Cl, Br, and I) in enriched-mantle melts from Pitcairn and Society seamounts. *Chem. Geol.* **2014**, *370*, 69–81. [CrossRef]
77. Zhang, Z.W.; Yang, X.Y.; Dong, Y.; Zhu, B.Q.; Chen, D.F. Molybdenum deposits in the eastern Qinling, central China: Constraints on the geodynamics. *Int. Geol. Rev.* **2011**, *53*, 261–290.
78. Grare, A.; Benedicto, A.; Mercadier, J.; Lacombe, O.; Trave, A.; Guilcher, M.; Richard, A.; Ledru, P.; Blain, M.; Robbins, J.; et al. Structural controls and metallogenic model of polyphase uranium mineralization in the Kiggavik area (Nunavut, Canada). *Miner. Depos.* **2021**, *56*, 1263–1296.